

UC Santa Barbara

UC Santa Barbara Previously Published Works

Title

Simple peptide coacervates adapted for rapid pressure-sensitive wet adhesion.

Permalink

<https://escholarship.org/uc/item/5hg4q15x>

Journal

Soft matter, 13(48)

ISSN

1744-683X

Authors

Kaminker, Ilia
Wei, Wei
Schrader, Alex M
et al.

Publication Date

2017-12-01

DOI


10.1039/c7sm01915g

Peer reviewed



Cite this: *Soft Matter*, 2017, 13, 9122

Simple peptide coacervates adapted for rapid pressure-sensitive wet adhesion†

Ilia Kaminker,[†] Wei Wei,[‡] Alex M. Schrader,^c Yeshayahu Talmon,^d Megan T. Valentine,[†] Jacob N. Israelachvili,^{b,c,f} J. Herbert Waite^{b,f,g} and Songi Han[†] 

We report here that a dense liquid formed by spontaneous condensation, also known as simple coacervation, of a single mussel foot protein-3S-mimicking peptide exhibits properties critical for underwater adhesion. A structurally homogeneous coacervate is deposited on underwater surfaces as micrometer-thick layers, and, after compression, displays orders of magnitude higher underwater adhesion at 2 N m⁻¹ than that reported from thin films of the most adhesive mussel-foot-derived peptides or their synthetic mimics. The increase in adhesion efficiency does not require nor rely on post-deposition curing or chemical processing, but rather represents an intrinsic physical property of the single-component coacervate. Its wet adhesive and rheological properties correlate with significant dehydration, tight peptide packing and restriction in peptide mobility. We suggest that such dense coacervate liquids represent an essential adaptation for the initial priming stages of mussel adhesive deposition, and provide a hitherto untapped design principle for synthetic underwater adhesives.

Received 22nd September 2017,
Accepted 16th November 2017

DOI: 10.1039/c7sm01915g

rsc.li/soft-matter-journal

Introduction

Soft load-bearing materials in living organisms have evolved structure–property relationships that are optimally adapted for function and organism survival. The dynamic processes for forming these materials from fluidic precursors show equally important adaptations that are strongly influenced by how rapidly the material needs to be deployed. Time to deployment typically requires days to months for the formation of tendons,¹ cartilage^{2,3} and hair,⁴ and involves a precise cell-mediated molecular self-assembly that is spatially and temporally controlled. This deployment time is too long for materials such as spider and silkworm silk,⁵ mussel byssus,⁶ and trematode egg capsules⁷ that

are recruited into function within seconds or less of being formed. These “on demand” materials are typically formed from metastable complex fluids by bioprocessing that resembles spinning, extrusion, or reaction injection molding. Given the tremendous importance of controlled multi-scale condensation of solution state macromolecules to soft materials⁸ and the parallels between, say spinning synthetic polymer hot melts and silk formation, it behooves investigators to look at the range of properties and functions of complex fluids used to make rapidly available load-bearing structures.

Since 1995, adhesion research has emphasized primarily interfacial chemistry, such as the role of DOPA and DOPA-inspired chemical moieties.⁹ The relevance of this emphasis was brought into question by the recent discovery that interfacial chemistry provides less than 0.01% of the adhesion energy contributed by plaque geometry and architecture in whole plaques.^{10,11} Here, we look at mussel and sandcastle worm adaptations beyond interfacial chemistry at the molecular scale. These marine organisms exploit spontaneous condensation of charged polypeptides by liquid–liquid phase separation or coacervation into complex liquids to form underwater adhesives. Sandcastle worms employ a complex coacervate, formed from a mixture of oppositely charged proteins as the mortar for building concrete tubes out of sand grains and shell fragments.¹² Other well-defined polymer-rich coacervate droplets are postulated to be essential for efficient delivery and deposition of the mussel foot proteins (mfp),¹³ as schematically depicted in Fig. 1a and b. These findings inspire our quest to identify coacervate liquids

^a Department of Chemistry and Biochemistry, University of California Santa Barbara, CA 93106, USA. E-mail: songi@chem.ucsb.edu

^b Materials Research Laboratory, University of California Santa Barbara, CA 93106, USA

^c Department of Chemical Engineering, University of California Santa Barbara, CA 93106, USA

^d Department of Chemical Engineering and the Russell Berrie Nanotechnology Institute (RBNI), Technion-Israel Institute of Technology, Haifa 3200003, Israel

^e Department of Mechanical Engineering, University of California Santa Barbara, CA 93106, USA

^f Biomolecular Science and Engineering Program, University of California Santa Barbara, CA 93106, USA

^g Department of Molecular, Cell and Development Biology, University of California, Santa Barbara, CA 93106, USA

† Electronic supplementary information (ESI) available. See DOI: 10.1039/c7sm01915g

‡ These authors contributed equally to this work.

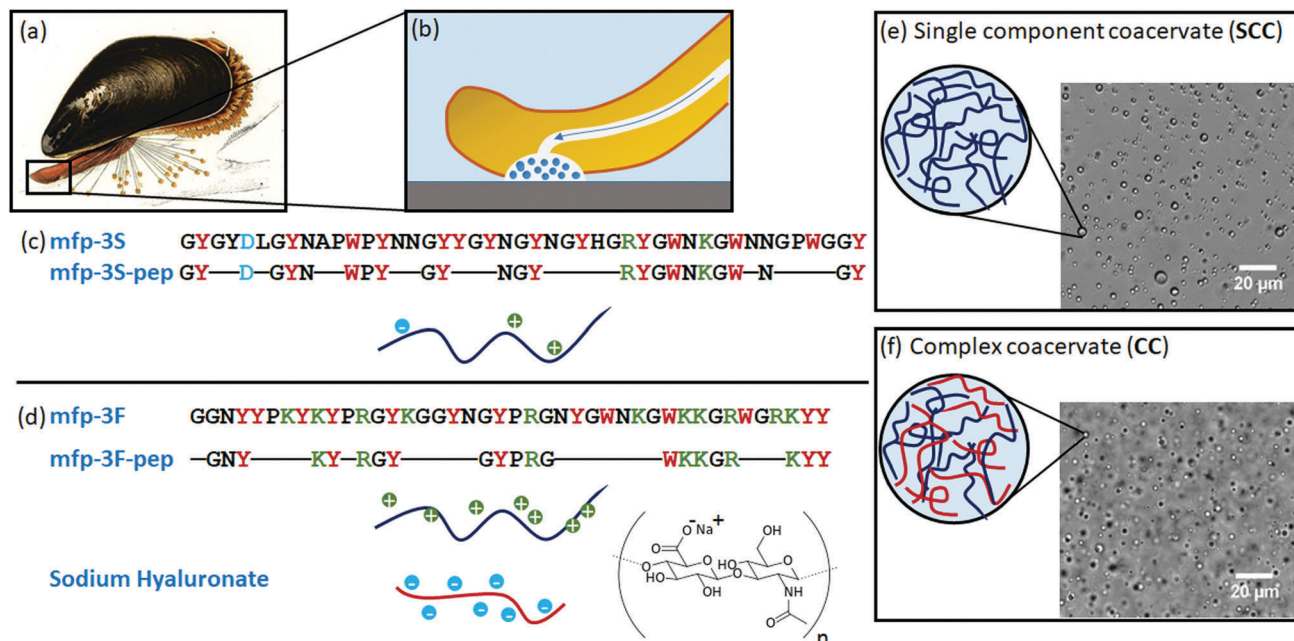


Fig. 1 (a) Mussel adhesive plaque formation. (b) Schematic representation of the plaque formation under the mussel foot. Coacervate droplets are shown in blue; an arrow shows the direction of material flow upon plaque deposition. Sequences of the (c) mfp-3S and mfp-3S-pep and (d) mfp-3F, mfp-3F-pep and hyaluronic acid (HA). Hydrophobic, positively and negatively charged amino acids are highlighted in red, green, and blue, respectively. Bright-field light micrographs together with the proposed schematics of the (e) single-component coacervate (SCC) and (f) complex coacervate (CC) phase, showing liquid–liquid phase separation with the appearance of droplets.

that may display significant and intrinsic adhesive properties in the presence of water and ions, without the need to wait for post-deposition curing or cross linking. Achieving this would present a milestone in enabling practical wet adhesion, where it is impossible to wait for full cure, for example for an adhesive joint that is submerged in water and immediately subjected to mechanical strain. The key is to design materials endowed with properties conducive with delivery and bonding to the surface as well as instant load-bearing and, when appropriate, permanent curing. We look to coacervation of mussel foot protein-inspired polypeptides.

In nature, different mfp-3 variants are among the first proteins to be deposited during mussel plaque formation and are found predominantly at the plaque surface interface.^{14,15} Recently, it was found that mfp-3S (termed “slow” for its slow electrophoretic migration) undergoes what is known as simple coacervation,¹⁶ in which high density polymer-rich droplets are formed in the absence of another polypeptide partner at low pH and high salinity (0.6 M).¹⁷ We will refer to the simple coacervation henceforth as single-component coacervation (SCC) for clarity. Inspired by this property, we set out to explore the adhesive and rheological properties of an mfp-3S inspired peptide analog, mfp-3S-pep, that was recently shown to replicate the simple coacervation behavior.¹⁸ Our hypothesis is that the coacervate phase, apart from facilitating deposition, contributes to plaque adhesion through favorable mechanical properties of this dense and viscous liquid, and therefore may be essential for priming the adhesion, and even providing load-bearing during the first stages of mussel plaque formation. We characterize the rheological,

structural and adhesive properties of the single-component coacervate composed solely of mfp-3S-pep, and compare its properties to that of a prototypical complex coacervate (CC) formed by a different mfp-3 related peptide mfp-3F-pep (F for “fast electrophoretic migration”). The complex coacervate was formed from a mixture of mfp-3F-pep with hyaluronic acid (HA), following a strategy used for obtaining the complex coacervate of a chimeric mfp-151 protein and HA.¹⁹

We report here that micrometer-thick layers of simple coacervate formed by spontaneous coacervation of synthetic mfp-3S-pep from bulk water, when deposited on surfaces yield effective adhesion forces that significantly outperform even the most adhesive mussel foot protein studied to date, mfp-5, as well as other biomimetic synthetic polymers that form thin layers on surfaces.^{20–22} In-addition we observed intriguing, previously unreported, effects where the mfp-3S-pep adhesion is enhanced by greater compression or longer compressive load times resembling the properties of pressure sensitive adhesives. In contrast, the mfp-3F-pep/HA complex coacervate exhibited only moderate improvement in the measured adhesive forces upon surface deposition, or compression, and displayed a set of physical properties that make this liquid more suitable for coating rather than adhesion applications. We performed a set of systematic physical characterizations of these complex liquids from the molecular to the macroscopic scale to reveal the structural, dynamic and mechanical basis for these dramatically contrasting properties. Our study concludes that highly efficient underwater adhesion can be achieved using single component coacervates with extremely high viscosities that lend themselves

to instant and efficient, albeit temporary, load bearing. Crucial for materials design, these adhesion-adapted properties become evident upon coacervation and, in the case of mfp-3S-pep, are intrinsically dependent on the amino acid sequence.

Results and discussion

The two different coacervates were prepared using synthetic analogs of the two mussel adhesive proteins involved in the first stages of the mussel plaque formation (Fig. 1a and b). These two peptides designed from the mussel foot proteins mfp-3F and mfp-3S^{23,24} are referred to here as mfp-3S-pep and mfp-3F-pep, respectively (see Fig. 1c and d). The mfp-3S-pep coacervate phase can form across a rather broad range of conditions, such as pH 3–8.5 and ionic strength of 0.6 M NaCl or pH 7–8.5 and ionic strength of 0.1 M NaCl.¹⁸ We focus on the condition of pH 3 and 0.6 M NaCl, as low pH and high ionic strength resemble the biological conditions for mussel plaque deposition.^{6,18} In contrast to the SCC of mfp-3S-pep, the net positively charged mfp-3F-pep forms a CC phase upon complexation with the polyanion, HA. The CC formation was found to be

optimal at an equimolar (which for these materials corresponds also to 1 : 1 positive to negative charge ratio) mixture of mfp-3F-pep and HA at pH 5 and ionic strength of 10 mM NaCl.

Under appropriate conditions, both systems undergo liquid–liquid phase separation, and the solution appears turbid to the naked eye. Bright-field light microscopy shows that the turbidity in both cases is a result of phase separation into polymer-rich droplets with diameters up to a few micrometers and a surrounding dilute phase (Fig. 1e and f). The liquid nature of the polymer-rich coacervate phase was confirmed by observing coacervate droplet fusion by confocal microscopy. The dark out-of-focus patches in the bright-field micrographs of the CC droplets are due to droplets that burst upon contact with the glass surface of the microscopy cover slip.

The adhesive properties of both types of coacervate liquids were measured using a Surface Forces Apparatus (SFA). In this experiment, the freshly mixed coacervate suspension was deposited between two mica surfaces (left panel in Fig. 2a). The coacervate was allowed to equilibrate for 60 minutes before beginning the experiment. This time was needed to ensure formation of a continuous layer of a coacervate film on the lower mica surface by gravity sedimentation. The upper mica

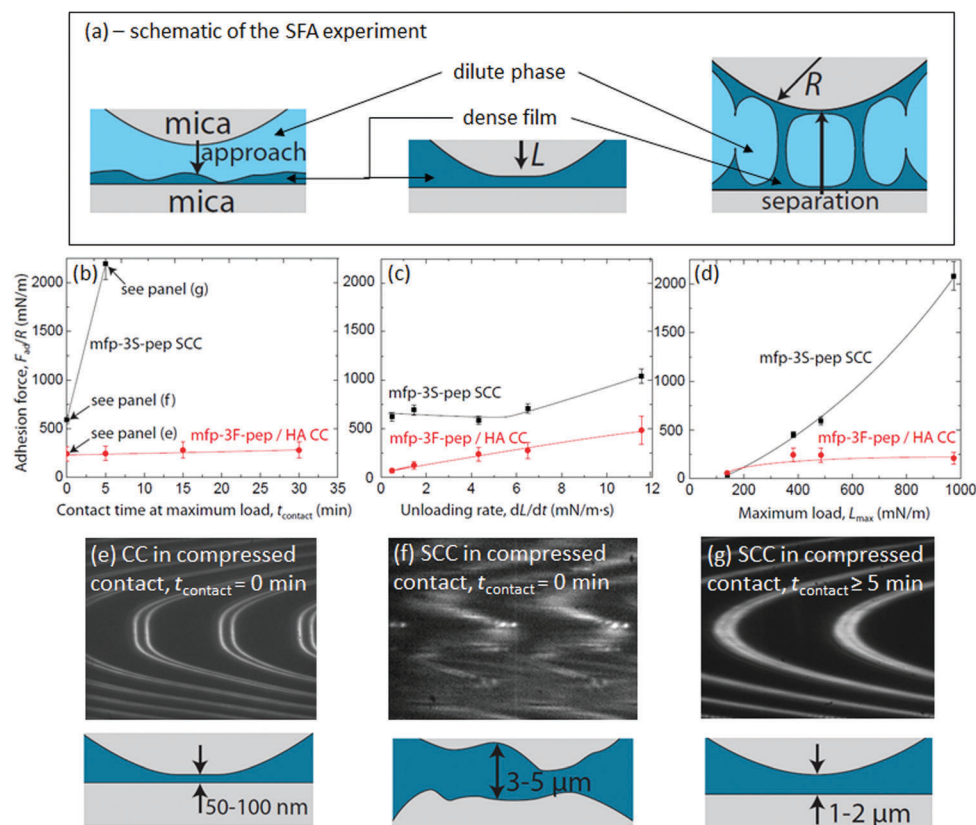


Fig. 2 SFA measurements of adhesion forces of mica surfaces across the mfp-3S-pep SCC and mfp-3F-pep/HA CC liquids. (a) Schematic of the SFA experiment: approach (left), compression (center), and separation of the surfaces (right). (b) Adhesion force as a function of contact time (constant unloading rate and maximum load of $4.3 \text{ mN m}^{-1} \text{ s}^{-1}$ and 480 mN m^{-1} , respectively), (c) adhesion force as a function of the unloading rate (while keeping the contact time and maximum load constant at 0 min and 480 mN m^{-1} , respectively), and (d) adhesion force as a function of maximum load (constant contact time and unloading rate of 0 min and $4.3 \text{ mN m}^{-1} \text{ s}^{-1}$, respectively). Characteristic FECO images and corresponding schematics for the (e) CC in compressed contact, (f) SCC in contact at short times ($t_{contact} = 0$ min in this case), and (g) SCC in contact for ≥ 5 min or at compressive loads of $\geq 1000 \text{ mN m}^{-1}$.

surface was brought into contact with the coacervate film, loaded further until the desired maximum compression was reached (middle panel in Fig. 2a), and subsequently unloaded at the same rate as it was loaded. The mica–mica separation distance at maximum compression (*i.e.*, the compressed coacervate film thickness) was measured using optical (FECO) interferometry.²⁵ The maximum compressive load, L_{\max} (middle panel in Fig. 2a) and the adhesion force, F_{ad} , upon separating the surfaces (right panel in Fig. 2a) were measured using a strain gauge (independent of the interferometry). All measured forces are in the normal direction (as opposed to shear forces). Note that the forces measured by the SFA are normalized by the radius of curvature, R , of the cylindrical disks ($R \sim 2$ cm) that are used as the substrates in the measurement, since surface forces between curved surfaces scale with the radius of curvature. Due to the turbidity of the deposition mixtures/suspensions, light could not adequately pass through the turbid suspension and interferometry could not be used to measure the separation distance between the mica surfaces until large compressions/loads were reached. Large compressions resulted in (i) a decrease of the coacervate film thickness, and (ii) squeezing out of the dilute/suspension phase that scattered light, both of which made interferometry possible at large loads. Generally, interferometry was only possible at mica–mica separations < 5 μm . The adhesive jump out, corresponding to the snapping of capillary bridges of dense coacervate liquid (right panel in Fig. 2a), occurred at separations larger than 5 μm , which prevented the creation of complete force *vs.* distance curves.

The adhesion force for the CC liquid is independent of contact time, whereas that for the SCC increases sharply with contact time (Fig. 2b), reaching an impressive value of 2 N m^{-1} after 5 minutes of contact. Longer compression times resulted in continued increase in the adhesion force, beyond what can be measured using an SFA. The difference in the contact time dependence suggests that the CC film relaxes more quickly under compression than the SCC film. This comparison is further shown in the FECO images (Fig. 2e–g). Upon initial compression to $L_{\max} = 480$ mN m^{-1} between the two mica surfaces, the CC liquid forms a thin (50–100 nm), smooth layer (Fig. 2e). In contrast, the SCC initially forms a rough, thick (3–5 μm) layer (Fig. 2f), but the layer thins (to 1–2 μm) and becomes smooth after 5 minutes of contact time under a strong compressive load of 480 mN m^{-1} (Fig. 2g). Note that the schematic drawn in panel 2f indicates that the jagged fringes are primarily a result of surface roughness, as opposed to an inhomogeneous refractive index within the film (*i.e.*, pockets of the dilute phase). This is because the odd (left) and even (right) fringes have the same shape and dimensions (within error), which would not be the case if the refractive index of the film varied across the contact region.²⁶ However, given the quality of the FECO image, the existence of small quantities of the dilute phase cannot be entirely ruled out.

Across a range of unloading rates, the mfp-3S-pep SCC consistently displayed much higher adhesion values than the mfp-3F-pep/HA CC (Fig. 2c). The measured adhesion forces increased monotonically for the CC with increasing unloading rates from 0.5 to 11.6 $\text{mN m}^{-1} \text{s}^{-1}$. As shown in Fig. 2c (red data points),

we did not observe a leveling off of the adhesion force at low unloading rates, indicating that an equilibrium adhesion force was never reached. Unloading rates smaller than $dL/dt = 0.5$ $\text{mN m}^{-1} \text{s}^{-1}$ (or speeds < 10 nm s^{-1}) were not attainable with our SFA setup due to the use of a stiff “helical spring” that connects the cantilever base to the motorized micrometer, which was required to control the cantilever height in order to achieve a particularly wide range of separation values across a several μm -thick film.

For the SCC, the adhesion forces again increased monotonically between unloading rates from 4.3 to 11.6 $\text{mN m}^{-1} \text{s}^{-1}$, but were found to be invariant between 0.5 and 4.3 $\text{mN m}^{-1} \text{s}^{-1}$ – over which range the adhesion force remained $F_{\text{ad}} \sim 625$ mN m^{-1} . However, the adhesion force increases with increasing contact time for the SCC (Fig. 2b), raising the possibility that the apparently invariant adhesion forces with decreasing unloading rates may still be associated with decreasing adhesion forces for the SCC, when accounting for the effect that smaller unloading rates necessarily correspond to increased contact time. A strong dependence of the adhesion force on unloading/separation rate is commonly seen in adhesion studies on coacervate films. Peptide or polymer chains within the film can disentangle (or relax) more naturally when small unloading rates are applied²⁷ resulting in lower adhesion forces. Using a CC phase made of mfp/HA, Hwang *et al.* reported adhesion forces of 7–36 mN m^{-1} as the unloading rate increased from 0.1 to 1 $\text{mN m}^{-1} \text{s}^{-1}$.²⁸ With a polylysine/poly(glutamic acid) CC phase, Priftis *et al.* reported adhesion forces of 4–30 mN m^{-1} over separation rates ranging from 2.4 to 33.2 nm s^{-1} (roughly 0.1 to 1.5 $\text{mN m}^{-1} \text{s}^{-1}$).²⁹ Our adhesion values of 70 mN m^{-1} for the CC and 625 mN m^{-1} for the SCC phase at an unloading rate of 0.5 $\text{mN m}^{-1} \text{s}^{-1}$ (the smallest unloading rate we measured) are still substantially larger than those reported in the literature, and especially so for the SCC phase, which is larger by 1–2 orders of magnitude compared to previously reported adhesion forces for other coacervates. While this may be partially due to differences in the loads applied, for the mfp-3S-based SCC coacervate, we attribute the larger than an order of magnitude difference predominantly to the spontaneous deposition property of the coacervate liquid onto surfaces, out of bulk water, into much thicker, viscous liquids than have previously been observed with other coacervates liquids^{28,29} – a property engrained in the mfp-3S-pep sequence.

Similarly, distinct trends in adhesive behavior for the two coacervate systems were observed when the maximum load, instead of the contact time, was varied (Fig. 2d). Upon initial increase from 140 mN m^{-1} to 390 mN m^{-1} , we observed an increase in the apparent adhesion force with both coacervate systems. However, no further change in the adhesion force was observed with the CC on increasing the maximum compressive load from 390 mN m^{-1} to 1000 mN m^{-1} . In contrast, the SCC showed a steep increase in the measured adhesion force for the whole range of applied loads, eventually reaching values of > 2 N m^{-1} that correspond to the maximum values measurable by an SFA, suggesting that even higher adhesion forces may be possible. Under nearly all conditions tested, the SCC produced higher adhesion forces than its CC counterpart. Notably, these

large adhesion forces were achieved by simply compressing the coacervate phase between two wet surfaces submerged in water, and only required the formation of a continuous layer of a coacervate condensate in contact with both mica surfaces, but no curing nor cross-linking. Strong increase in the adhesion force with increase in time in contact, compression load and unloading rate are hallmarks of pressure-sensitive adhesives,³⁰ thus suggesting that the mfp-3S-pep SCC can be classified as an underwater pressure-sensitive adhesive material. These unusual properties of the mfp-3S-pep SCC, together with profound differences compared to the properties of the mfp-3F-pep/HA CC led us to investigate the interaction of the coacervate liquid with surfaces in greater detail.

Confocal microscopy was used to visualize coacervate droplets interacting with a glass surface. Here, a droplet of freshly formed coacervates, prepared with a nonspecific protein-binding dye, was deposited on a clean microscopy cover slip and the inverted microscope focused on the glass/water interface to visualize the droplets that were gravity-sedimented onto the glass surface. Three orthogonal projections of the 3D confocal micrographs of mfp-3F-pep/HA CC and mfp-3S-pep SCC coacervates are shown in Fig. 3a and b, respectively. The confocal images reveal that the mfp-3F-pep/HA CC droplets readily spread upon contact with a glass surface (Fig. 3a), whereas the mfp-3S-pep SCC droplets largely retain their spherical shape, even after extended waiting times of > 30 min (in Fig. 3b, a corona is visible around most of the droplets, characteristic of a retained 3D curvature). This supports the interpretation drawn from the FECO patterns that the mfp-3F-pep/HA CC liquid displays superior coating properties and easily forms a smooth continuous layer, whereas the mfp-3S-pep SCC liquid forms a continuous layer only after compression, indicating stronger internal cohesive energy is holding together the mfp-3S-pep SCC phase compared to the mfp-3F-pep/HA CC droplets. Notably, the differences in surface coating do not depend on the nature of the surface: qualitatively the same behavior was observed when hydrophobic (alkylated) glass was used for deposition of the coacervate liquids (Fig. S1, ESI†). Thus, the dramatic difference in spreading tendency on a solid surface represents a materials property intrinsic to these coacervate liquids. It is important to remember that the mfp-3S-pep

coacervate is still clearly a liquid phase, as verified by observing seamless fusion of two coacervate droplets into a larger one. (A movie showing two merging SCC droplets taken with a time-lapse series of confocal images is available in the ESI†).

The shape persistence of the droplets on solid surfaces, irrespective of the solid surface's hydrophobicity, shows that the much stronger cohesive energy of the mfp-3S-pep SCC phase as compared to the mfp-3F-pep/HA CC phase is a major factor in their different properties, and also implies higher viscosity for the SCC phase compared to its CC counterpart. To obtain a quantitative measure of the viscosity difference between the two coacervate liquids, microrheology measurements were performed using 40 nm fluorescent beads (FluoSpheres[®], 0.04 μm , (565/580), ThermoFisher Scientific) as tracers.^{31,32} The thermally induced motion of the tracer beads was analyzed and a viscosity of $\eta = 19.4 \pm 0.3$ Pa s found for the mfp-3F-pep/HA based CC, which corresponds to a 4 orders of magnitude higher viscosity compared to that of a dilute aqueous solution ($\eta \sim 1$ mPa s for pure water); such viscosity is, for example, observed for a 50% w/w PEG1000 aqueous solution at room temperature with $\eta = 24.3$ Pa s.³³ In contrast, no resolvable motion was observed for the tracers embedded in the mfp-3S-pep coacervate phase, indicating even higher viscosity for the SCC phase. In this case, only the lower viscosity limit could be determined to be at $\eta > 1200$ Pa s. Such viscosity is comparable to that of molten glasses ($\eta = 10^2$ – 10^4 Pa s), and exceeds that of the mfp-3F-pep/HA coacervate by at least 2 orders of magnitude. Details of the microrheology procedure and a sample movie showing the tracer motion in both coacervates are available in the ESI†.

Such dramatic differences in both the adhesive and rheological properties motivated us to explore the differences in sub-micrometer structure of these different complex liquids by cryo-transmission electron microscopy (cryo-TEM). The resulting images show significant differences between the SCC and CC phases (Fig. 4). The mfp-3F-pep/HA CC shows sheet-like structures with ill-defined boundaries, spreading over distances of several micrometers (marked with large white arrow in Fig. 4a). The large blue arrow on Fig. 4a points to a region of a dilute phase. The CC phase does not appear to interact preferentially with the perforated carbon support grid (marked with orange arrows). In Fig. 4b small coacervate droplets were observed inside the same field of view together with the continuous sheets. The internal morphology of the two (large white arrows in Fig. 4b) appears to be the same, displaying heterogeneity at the ~ 5 nm length scale, which becomes especially apparent when the same droplet is viewed at higher magnification (inset in Fig. 4b). In fact, heterogeneities within the coacervate liquid are quite common in the dense phase of complex coacervates with low interfacial energies.^{19,28,34,35}

The mfp-3S-pep SCC, when vitrified using the same procedure, does not form extended and unsupported coacervate sheets of materials. Instead, it appears to strongly interact with the perforated carbon support grid, forming ~ 50 – 100 nm wide layers in contact with the surface (small white arrows in Fig. 4c). Furthermore, several structures with well-defined droplet shapes were observed in the same field of view (large arrows in Fig. 4c). Many of the mfp-3S-pep SCC droplets display a faint

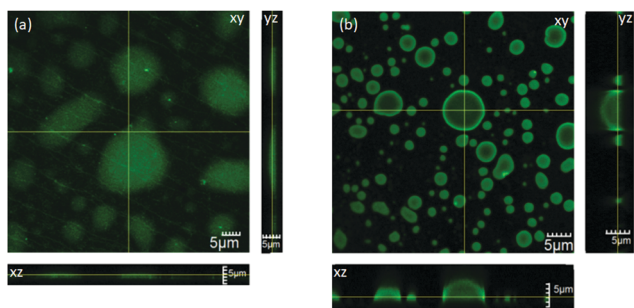


Fig. 3 Orthogonal views representation of the 3D confocal micrographs of mfp-3F-pep/HA complex coacervate (a) and mfp-3S-pep single component coacervate (b) deposited on a glass surface. The samples shown were allowed to settle for ~ 30 min prior to imaging. Yellow lines denote the positions of the cross sections in other views.

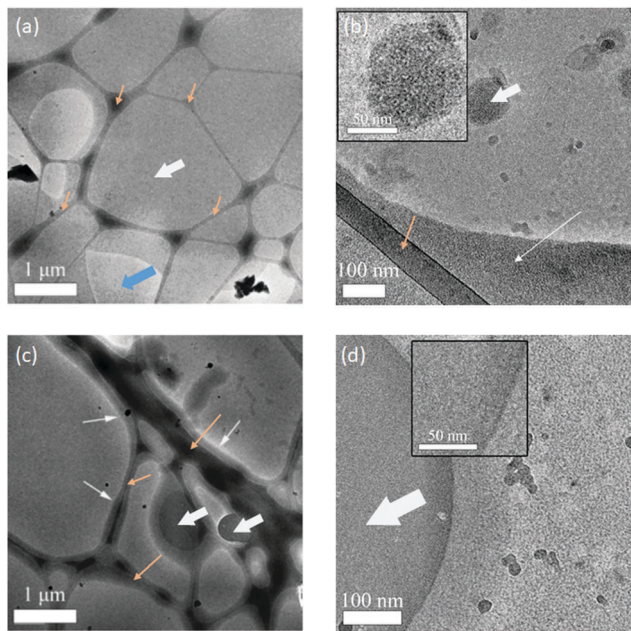


Fig. 4 Cryo-TEM micrographs for mfp-3F-pep/HA complex coacervate with 30 s on-the-grid mixing time (a and b) and mfp-3S-pep single-component coacervate with 60 s on-the-grid mixing time (c and d). Orange arrows denote the substrate (perforated carbon film). Thick white arrow in (a) points to the dense coacervate phase, blue arrow points to a region of the dilute phase. In (b) thick white arrow points to the coacervate droplet shown in the inset; thin white arrow points to the continuous coacervate layer. In (c) thin white arrows point to the coacervate layer adherent to the perforated carbon support grid; in (c and d) thick white arrows point to the coacervate droplets; black triangles in (d) point to the faint corona.

corona, which was especially pronounced in the higher magnification micrographs (Fig. 4d). This suggests that the coacervate droplets maintained their 3D curvature upon contact with the surface instead of readily spreading over the surface, consistent with observations by confocal imaging (Fig. 3b). The cryo-TEM micrographs again highlight the strongly cohesive interactions within the mfp-3S-pep SCC phase, while also demonstrating the tendency of mfp-3S-pep SCC to form strong adhesive interactions with the perforated carbon support surface.

Interestingly, when imaged at higher magnification, the mfp-3S-pep droplets show a homogeneous interior (Fig. 4d), lacking the ~ 5 nm heterogeneity observed in the mfp-3F-pep/HA CC phase. The lack of the characteristic nanostructure in the highly cohesive (and adhesive) mfp-3S-pep SCC phase (inset in Fig. 4d), compared to the mfp-3F-pep/HA CC phase (inset in Fig. 4b) is intriguing, since it suggests that efficient energy dissipation and adhesion at the micrometer length scale can be achieved without, or prior to, formation of the intricate load-bearing structures at the nanometer to sub-micrometer scale that are typically observed in mature mussel plaques, including filaments or mesh structures.¹¹

Since no chemical cross-linking takes place, the unusually high cohesive energy of the mfp-3S-pep SCC liquid must be due to the molecular self-interaction of the peptide molecules within the coacervate phase. To investigate the molecular underpinnings of

the adhesive and rheological properties of the mfp-3S-pep CC, and to contrast it with that of mfp-3F-pep/HA SCC, we employed electron paramagnetic resonance (EPR) and Overhauser dynamic nuclear polarization (ODNP) spectroscopies of spin-labeled mfp-3 peptides or spin-labeled HA polymers, in separate experiments. Nitroxide radical-based 1-oxyl-2,2,5,5-tetramethylpyrrolone-3-methyl)methanethiosulfonate (MTSSL) spin labels were attached to strategically placed cysteine residues of the peptide. The spin-labeled versions of the two peptides are referred to as mfp-3F-pepSL and mfp-3S-pepSL for spin labeling in the middle of the sequence, mfp-3S-pepSL2 for N-terminal spin labeling, and HA-SL for the spin-labeled version of the HA polymer (the peptide sequences are given in Table S1 in ESI[†]). To ensure that an increase in spin-spin interactions from an increase in local spin concentrations upon formation of the condensed coacervate phase does not affect the EPR spectra of the peptides, a “spin dilution” scheme was used for sample preparation, where only 20% of peptides in mfp-3F-pep/HA and 10% in mfp-3S-pep were spin labeled. The spin labeling did not affect the coacervate formation, as was judged by the identical turbidity (measured *via* light scattering at $\lambda = 600$ nm) of the coacervates formed with and without the labeled peptides. Differences in the peptide dynamics resulted in spectrally distinct EPR lineshapes, permitting us to resolve and quantify the spectral components of the peptides partitioned in the coacervate, including the rotational correlation time τ_{rot} of the spin labels and their relative abundance. Thus EPR spectroscopy offers a direct means to study coacervate-internal properties at the molecular level, unobscured by the peptide population remaining in the dilute phase.

For both mfp-3S-pepSL and mfp-3F-pepSL, the EPR spectra before the corresponding coacervate formation consisted of a single spectral component (Fig. S3a and b, ESI[†]), displaying high mobility ($\tau_{\text{rot}} \approx 0.1$ ns) as typically observed for unstructured peptides in solution state.³⁶ Upon coacervate formation, a second “slow” spectral component appears (Fig. S4a and b, ESI[†]) that corresponds to a peptide population with restricted rotational mobility of its spin label. Importantly, this “slow” component assigned to the peptides in the coacervate phase encompasses nearly the entire peptide population (95% in case of mfp-3S-pepSL and 85% in case of mfp-3F-pepSL/HA,) as summarized in Fig. 5a. The remaining “fast” peptide population displays mobility similar to that of the peptides prior to coacervate formation, and thus represents peptides in, or exchanging with, the equilibrium dilute phase upon coacervate formation. The slowdown of the peptide dynamics is quantified as a retardation factor defined as the ratio of the spin-label rotational correlation times in the coacervate and in the dilute phase prior to coacervation: $\tau_{\text{rot}}/\tau_{\text{rot(dilute)}}$. Interestingly, the slowdown of peptide dynamics in the mfp-3S-pepSL SCC is an order of magnitude greater (retardation factor of 200; $\tau_{\text{rot}} \sim 20$ ns) than in the mfp-3F-pepSL/HA CC (retardation factor of 10; $\tau_{\text{rot}} \sim 1$ ns), as summarized in Fig. 5b. Moreover, no slowdown of the spin probe of HA-SL was observed upon mfp-3F-pep/HA-SL CC formation (Fig. S5, ESI[†]), suggesting that the compaction of HA and interaction between mfp-3F-pepSL and HA is very weak even in the coacervate phase.

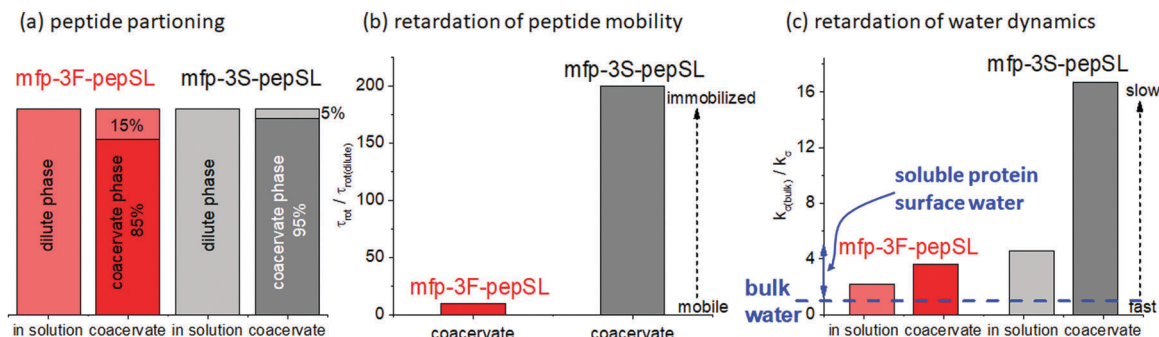


Fig. 5 (a) Peptide partitioning between the coacervate and dilute phases and (b) retardation in peptide mobility in the coacervate phase as derived from EPR spectroscopy. (c) Water retardation before and upon coacervate formation as obtained from ODNP measurements.

The latter observation is consistent with previous reports of similar complex coacervate systems consisting of mfp151 and spin-labeled HA.¹⁹

A molecular level understanding of a condensate is not complete without insight into the constituents' hydration and interfacial water. The surface water dynamics of the mfp-3 peptides was characterized through the measurement of cross-relaxivity, k_{σ} , between a nitroxide radical-based spin label tethered to the peptide surface (same spin label as used for EPR) and the surrounding water by Overhauser Dynamic Nuclear Polarization (ODNP) at 0.35 T.³⁷ The value of k_{σ} is modulated by the diffusive motion of water protons relative to the motion of the spin label within close (5–15 Å) proximity, where higher k_{σ} values correspond to faster water diffusion in the vicinity of the spin label, and *vice versa*.³⁸ The retardation in surface water diffusivity is given by the ratio of the relaxivity of bulk water ($k_{\sigma(bulk)} = 95 \text{ s}^{-1} \text{ M}^{-1}$) and of hydration water near the peptide surface, as $k_{\sigma(bulk)}/k_{\sigma}$. In dilute solution prior to coacervate formation, this retardation factor, $k_{\sigma(bulk)}/k_{\sigma}$ was found to be 2.2 for the mfp-3F-pepSL surface, falling in a typical range for surface water diffusivity on solvent-exposed peptide or protein surfaces. In contrast, a retardation factor of $k_{\sigma(bulk)}/k_{\sigma} = 5$ was found for mfp-3S-pepSL, falling at the lower end of surface water diffusivity found on peptide surfaces in solution (Fig. 5c). Upon coacervation, the surface water diffusivity in both cases experiences significantly greater retardation, reaching $k_{\sigma(bulk)}/k_{\sigma} \sim 4$ and ~ 17 for mfp-3F-pepSL CC and mfp-3S-pepSL SCC, respectively (Fig. 5c). ODNP data thus reveal that the mobility of hydration water surrounding the peptide constituents is significantly restricted in the mfp-3S-pep SCC phase that we had confirmed to be composed of highly confined and motionally restricted peptide molecules. This property is in stark contrast to the wet and highly dynamic environment found within the mfp-3F-pep/HA CC phase that correspond to characteristics found in several other CC systems made of intrinsically disordered and charged biopolymers.^{19,39,40} Based on this, it is easy to suggest that the mfp-3S-pep SCC phase must be virtually dry, and on its way to forming a condensed solid gel. We examine this question by the direct measurement of the density of water near the peptide constituents upon coacervate formation by Electron Spin Echo Envelope Modulation (ESEEM) spectroscopy. We find that more than half of the water molecules that initially

solvate the peptide in the dilute phase are expelled upon mfp-3S-pepSL SCC formation (see ESI† for details of the ESEEM spectroscopy). This confirms that the coacervate interior is significantly, but by no means entirely, dehydrated, consistent with the coacervate being a liquid phase and its formation reversible. Analogous ESEEM measurements were not performed for the mfp3f-pep/HA coacervate, due to persistent sample decomposition upon freezing, which is required for ESEEM measurements. This may indicate that the interior of the mfp-3F-pep/HA CC phase is held by a weak and delicate balance of intermolecular interactions that may be easily perturbed by the freezing process. It emerges from EPR, ODNP and ESEEM spectroscopic studies that the high viscosity of the mfp-3S-pep SCC phase is a direct result of peptide packing, strong inter-peptide interactions and peptide dehydration, as manifested in the dramatic reduction of peptide mobility upon coacervate formation. This is in contrast to the wetter and more dynamic mfp-3F pep/HA CC phase. Still, based on the physical and molecular-level characterization, the mfp-3S-pep SCC is a viscous and dense liquid, not a solid.

Finally, to be able to control a wet adhesive system based on reversible coacervation, it is relevant to know the critical tuning knobs. Specifically, we test the temperature as a variable to see whether the mfp-3S-pep SCC formation exhibits upper critical solution temperature (UCST) or lower critical solution temperature (LCST) behavior, since the two imply different thermodynamic driving factors for coacervate formation. For this purpose, we monitored the stability and population of the dense and dilute phases of the mfp-3S-pepSL SCC as a function of temperature. The quantification of both the peptide partitioning and dynamics between the dense and dilute coacervate phase is achieved by EPR lineshape analysis. We find that mfp-3S-pep SCC formation exhibits clear UCST behavior. Accordingly, we see a concerted trend with the peptide partitioning shifting away from the coacervate towards the dilute phase (Fig. 6a), and the mobility of the peptides remaining in the coacervate phase increasing, as measured by the rotational correlation time of the peptide over that of free spin label, $\tau_{rot}/\tau_{rot(bulk)}$, with increasing temperatures (Fig. 6b). Note that since the partitioning and mobility of the two spin-labelled mfp3-S-pep variants was very similar the data presented in Fig. 6 are an average of the data acquired for the two peptide variants with individual data for mfp-3S-pepSL/mfp-3S-pepSL2 presented in Fig. S6 (ESI†). Critically, these

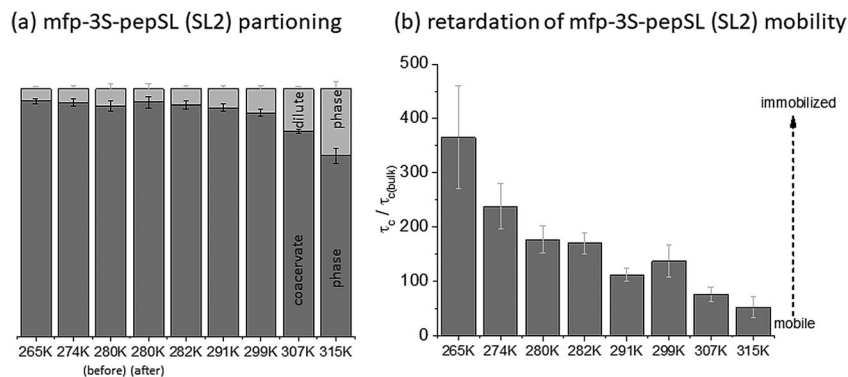


Fig. 6 EPR spectroscopy derived (a) mfp-3S-pepSL/mfp-3S-pepSL2 peptide partitioning between the coacervate and dilute phases and (b) peptide mobility presented as retardation factor in the coacervate phase as function of temperature. (Higher values correspond to slower peptide mobility.) The data presented in this figure are averaged from EPR measurements of the mfp-3S-pepSL and mfp-3S-pepSL2 coacervates and the error bars represent the standard deviation of the EPR parameters derived from those measurements.

temperature-induced changes are fully reversible without a notable hysteresis, as reflected in the indistinguishable EPR spectra taken before *vs.* after completing the temperature series. The overlay of the mfp-3S-pepSL EPR spectra acquired at 280 K “before” at the maximum temperature (315 K) and at 280 K “after” the temperature series are depicted in Fig. S7 (ESI[†]). The mfp-3S-pep, as well as the original mfp-3S protein sequences with their high glycine and proline content and overall negative hydrophathy (high hydrophobicity) fall within the proposed guidelines by Quiroz and Chilkoti⁴¹ who showed that zwitterionic peptides with high glycine and proline content and overall high hydrophobicity (negative hydrophathy on the Kyte–Doolittle scale⁴²) are predicted to exhibit UCST behavior, consistent with our findings, though they did not discuss the nature of the condensed phase below the upper critical temperature. (hydrophathy on Kyte–Doolittle scale is shown on Fig. S9, ESI[†]). However, the UCST behavior of mfp-3S-pep SCC is in striking contrast with the canonical single-component coacervate property of elastin that exhibits prototypical LCST behavior.⁴³ LCST behavior implies an entropy-driven process. In contrast, UCST behavior implies that favorable (negative) complexation enthalpy is the main driving force for mfp-3S-pep SCC formation, to which all inter-peptide attractive forces, such as electrostatic, H-bonding and van der Waals interactions contribute. At elevated temperatures these interactions become comparable to or smaller than the thermal energy term proportional to the entropy of the coacervate phase, thereby weakening the inter-peptide association and resulting in the dissolution of the coacervate phase.

Conclusion

In this work we presented a new system and process for efficient underwater adhesion based on spontaneous coacervate formation of a single peptide condensing from bulk solution. Specifically, the mfp-3S-inspired peptide undergoes spontaneous phase separation at low pH upon increase in ionic strength and forms a polymer-dense coacervate phase. This dense liquid readily deposits onto surfaces out of bulk water, while possessing

readily available underwater adhesive properties. The observed steep increase in the adhesion force with time in contact, compression load and unloading rate lead us to conclude that the adhesion properties of the mfp-3S-pep SCC are consistent with what is expected from the underwater pressure-sensitive adhesive. Significantly, the strong pull-off forces measured by SFA did not require any post-deposition curing, and only required formation of good contact between the mica surface and the coacervate that was achieved simply by modest compression of the mfp-3S-pep coacervate layer between two mica surfaces for several minutes. This implies that a more controlled deposition procedure can potentially significantly reduce the required time to form strong adhesion and further improve the adhesion force. The promising adhesive properties of mfp-3S-pep coacervate were traced to the very high viscosity of the still liquid SCC phase that we found to be rooted in strongly cohesive, enthalpy driven, peptide–peptide interactions, as reflected in significant motional confinement and dehydration of the mfp-3S-pep peptides upon coacervation.

We hypothesize that the high viscosity and strong cohesion of the mfp-3S-pep-based SCC liquid is essential for efficient wet adhesion, while the liquid nature of the coacervate phase ensures the ease of deposition and efficient contact formation between the adhesive material and the surface in the first stages of adhesive mussel plaque formation. This combination of properties – cohesion and interfacial adhesion – is also consistent with requirements for potential artificial underwater pressure-sensitive adhesives. Interestingly, this dual requirement is efficiently achieved by the mfp-3S-pep-based SCC liquid with no post-deposition curing, without the involvement of DOPA, and without the formation of structures on nanoscopic to microscopic length scales. These findings suggest that we may have successfully replicated a portion of the amazing adaptive capabilities of natural mussel foot systems, given that the native mfp-3S is the first protein secreted upon mussel plaque deposition, and that the conditions for mfp-3S SCC formation (low pH and high ionic strength) resemble conditions found under the mussel foot upon plaque formation. Further maturation of the native plaque occurs at later stages,

for example through iron-mediated DOPA cross linking and the formation of 3D microstructures, followed by formation of the larger scale overall plaque geometry adopted for efficient force redistribution and energy dissipation in the mature plaque. While the exact timescales for the maturation processes in the mussel adhesive plaques are not known, the rate of pH equilibration from low pH at plaque deposition to higher pH of the seawater⁶ suggests that the minutes timescale observed in the SFA experiment *in vitro* for achieving and maximizing the load-bearing properties of the mfp-3S_{pep} coacervate is a relevant one in nature. Significantly, these sets of favorable wet adhesion properties are encoded in the mfp-3S peptide's amino acid sequence and are achieved through a delicate balance between the hydrophobic, hydrogen bond, van der Waals and electrostatic interactions that are toggled by pH and temperature. The UCST behavior for the mfp-3S-pep SC formation suggests that these attractive interactions, not the increase in the system's entropy, are the main driving force for the coacervate formation. We believe that a single-component coacervate with strong inter-macromolecule cohesion can potentially revolutionize the design principles for synthetic underwater adhesives. Once the adhesive properties of the mfp-3S-pep SCC are replicated in an artificial polymer-based system, additional material properties can be installed, such as on-demand permanent curing that will ensure efficient and permanent bonds under harsh underwater environments.

Conflicts of interest

There are no conflicts of interest to declare.

Acknowledgements

The research reported here was primarily supported by the NSF MRSEC Program through DMR 1720256 (IRG-1). In addition JHW and JNI acknowledge the support by NIH grant R01 DE018468. Confocal micrographs were obtained in the NRI-MCDB microscopy facility; the spectral confocal microscope was funded by NIH grant 1 S10 OD010610-01A11; Dr Mary Raven is acknowledged for her help with acquisition of confocal images. The cryo-TEM work was performed at the Technion Center for Electron Microscopy of Soft Materials, supported by the Technion Russell Berrie Nanotechnology Institute (RBNI). We Thank Ms Judith Schmidt for her technical help with the cryo-TEM. IK acknowledges the support of the long-term postdoctoral fellowship by the Human Frontier Science Foundation.

References

- 1 K. L. Goh, D. F. Holmes, H.-Y. Lu, S. Richardson, K. E. Kadler, P. P. Purslow and T. J. Wess, *J. Biomech. Eng.*, 2008, **130**, 021011.
- 2 Y. Morita, N. Tomita, H. Aoki, M. Sonobe, S. Wakitani, Y. Tamada, T. Suguro and K. Ikeuchi, *J. Biomech.*, 2006, **39**, 103–109.
- 3 M. Ochi, Y. Uchio, K. Kawasaki, S. Wakitani and J. Iwasa, *J. Bone Jt. Surg.*, 2002, **84B**, 571–578.
- 4 J. W. S. Hearle, *Int. J. Biol. Macromol.*, 2000, **27**, 123–138.
- 5 F. Vollrath and D. P. Knight, *Nature*, 2001, **410**, 541–548.
- 6 N. R. M. Rodriguez, S. Das, Y. Kaufman, J. N. Israelachvili and J. H. Waite, *Biofouling*, 2015, **31**, 221–227.
- 7 J. S. Cordingley, *Parasitol. Today*, 1987, **3**, 341–344.
- 8 W. M. Aumiller, F. Pir Cakmak, B. W. Davis and C. D. Keating, *Langmuir*, 2016, **32**, 10042–10053.
- 9 J. H. Waite, *J. Exp. Biol.*, 2017, **220**, 517–530.
- 10 K. W. Desmond, N. A. Zaccchia, J. H. Waite and M. T. Valentine, *Soft Matter*, 2015, **11**, 6832–6839.
- 11 E. Filippidi, D. G. DeMartini, P. M. de Molina, E. W. Danner, J. Kim, M. E. Helgeson, J. H. Waite and M. T. Valentine, *J. R. Soc., Interface*, 2015, **12**, 20150827.
- 12 R. J. Stewart, J. C. Weaver, D. E. Morse and J. H. Waite, *J. Exp. Biol.*, 2004, **207**, 4727–4734.
- 13 D. R. Miller, S. Das, K.-Y. Huang, S. Han, J. N. Israelachvili and J. H. Waite, *ACS Biomater. Sci. Eng.*, 2015, **1**, 1121–1128.
- 14 B. P. Lee, P. B. Messersmith, J. N. Israelachvili and J. H. Waite, *Annu. Rev. Mater. Res.*, 2011, **41**, 99–132.
- 15 H. Zhao, N. B. Robertson, S. A. Jewhurst and J. H. Waite, *J. Biol. Chem.*, 2006, **281**, 11090–11096.
- 16 H. G. Bungenberg de Jong, *Colloid Sci.*, 1949, **2**, 335–432.
- 17 W. Wei, Y. Tan, N. R. Martinez Rodriguez, J. Yu, J. N. Israelachvili and J. H. Waite, *Acta Biomater.*, 2014, **10**, 1663–1670.
- 18 W. Wei, L. Petrone, Y. Tan, H. Cai, J. N. Israelachvili, A. Miserez and J. H. Waite, *Adv. Funct. Mater.*, 2016, **26**, 3496–3507.
- 19 J. H. Ortony, D. S. Hwang, J. M. Franck, J. H. Waite and S. Han, *Biomacromolecules*, 2013, **14**, 1395–1402.
- 20 E. W. Danner, Y. Kan, M. U. Hammer, J. N. Israelachvili and J. H. Waite, *Biochemistry*, 2012, **51**, 6511–6518.
- 21 S. Seo, S. Das, P. J. Zalicki, R. Mirshafian, C. D. Eisenbach, J. N. Israelachvili, J. H. Waite and B. K. Ahn, *J. Am. Chem. Soc.*, 2015, **137**, 9214–9217.
- 22 C. Zhong, T. Gurry, A. A. Cheng, J. Downey, Z. Deng, C. M. Stultz and T. K. Lu, *Nat. Nanotechnol.*, 2014, **9**, 858–866.
- 23 V. V. Papov, T. V. Diamond, K. Biemann and J. H. Waite, *J. Biol. Chem.*, 1995, **270**, 20183–20192.
- 24 W. Wei, J. Yu, C. Broomell, J. N. Israelachvili and J. H. Waite, *J. Am. Chem. Soc.*, 2013, **135**, 377–383.
- 25 J. Israelachvili, Y. Min, M. Akbulut, A. Alig, G. Carver, W. Greene, K. Kristiansen, E. Meyer, N. Pesika, K. Rosenberg and H. Zeng, *Rep. Prog. Phys.*, 2010, **73**, 036601.
- 26 E. E. Meyer, K. J. Rosenberg and J. Israelachvili, *Proc. Natl. Acad. Sci. U. S. A.*, 2006, **103**, 15739–15746.
- 27 J. N. Israelachvili, *Intermolecular and Surface Forces*, Academic Press, 2015.
- 28 D. S. Hwang, H. Zeng, A. Srivastava, D. V. Krogstad, M. Tirrell, J. N. Israelachvili and J. H. Waite, *Soft Matter*, 2010, **6**, 3232–3236.
- 29 D. Priftis, R. Farina and M. Tirrell, *Langmuir*, 2012, **28**, 8721–8729.
- 30 E. P. Chang, *J. Adhes.*, 1997, **60**, 233–248.
- 31 T. G. Mason, K. Ganesan, J. H. van Zanten, D. Wirtz and S. C. Kuo, *Phys. Rev. Lett.*, 1997, **79**, 3282–3285.
- 32 B. Schnurr, F. Gittes, F. C. MacKintosh and C. F. Schmidt, *Macromolecules*, 1997, **30**, 7781–7792.

- 33 P. Gonzalez-Tello, F. Camacho and G. Blazquez, *J. Chem. Eng. Data*, 1994, **39**, 611–614.
- 34 Y. Jho, H. Y. Yoo, Y. Lin, S. Han and D. S. Hwang, *Adv. Colloid Interface Sci.*, 2017, **239**, 61–73.
- 35 E. Kizilay, A. B. Kayitmazer and P. L. Dubin, *Adv. Colloid Interface Sci.*, 2011, **167**, 24–37.
- 36 M. Drescher, *EPR Spectroscopy*, Springer, Berlin, Heidelberg, 2011, pp. 91–119.
- 37 B. D. Armstrong and S. Han, *J. Am. Chem. Soc.*, 2009, **131**, 4641–4647.
- 38 J. M. Franck, A. Pavlova, J. A. Scott and S. Han, *Prog. Nucl. Magn. Reson. Spectrosc.*, 2013, **74**, 33–56.
- 39 K.-Y. Huang, H. Y. Yoo, Y. Jho, S. Han and D. S. Hwang, *ACS Nano*, 2016, **10**, 5051–5062.
- 40 R. Kausik, A. Srivastava, P. A. Korevaar, G. Stucky, J. H. Waite and S. Han, *Macromolecules*, 2009, **42**, 7404–7412.
- 41 F. G. Quiroz and A. Chilkoti, *Nat. Mater.*, 2015, **14**, 1164–1171.
- 42 J. Kyte and R. F. Doolittle, *J. Mol. Biol.*, 1982, **157**, 105–132.
- 43 D. W. Urry, T. L. Trapane and K. U. Prasad, *Biopolymers*, 1985, **24**, 2345–2356.